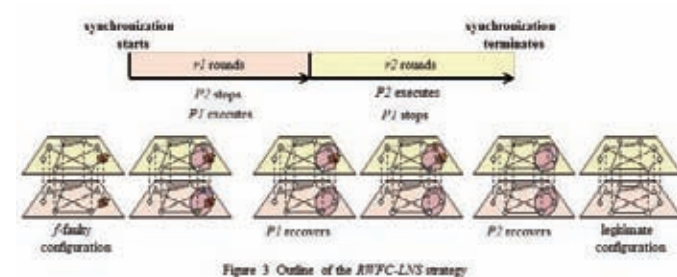


chronization protocol for the composition.

Before presenting the RWFC-LNS technique, we give the definitions of an *f*-fault-containing protocol and the measures for the fault-containment property. A configuration is *f*-faulty configuration if a legitimate configuration can be obtained by changing the states of *f* processes. To measure the containment property in recovery from *f*-faulty configurations, the recovery time and the contamination radius are considered. The recovery time is the time required to reach a legitimate configuration and the contamination radius is the maximum distance to a contaminated process from its nearest faulty process, where a contaminated process is the process that changes its state during the recovery. A self-stabilizing protocol is *f*-fault-containing if the recovery time and the contamination radius for any *f*-faulty configuration depend on *f* (not the total number of processes).

We show the outline of the RWFC-LNS technique for the composition of two self-stabilizing fault-containing protocols P1 and P2. In the following, let P1 be an *f*₁-fault-containing protocol with recovery time *r*₁ and the contamination radius *c*₁, and P2 be an *f*₂-fault-containing protocol with recovery time *r*₂ and the contamination radius *c*₂. As described below, the RWFC-LNS technique generates an *f*'-fault containing protocol composed from P1 and P2 where *f*' = min{*f*₁, *f*₂}.

Starting from an *f*'-faulty configuration, a process finding inconsistency in P1 or P2 initiates a self-stabilizing local neighborhood synchronizer. The local neighborhood synchronizer can synchronize timers at processes in the neighborhood of the initiator. Using the synchronized timer, each process in the contamination radius of P1 and P2 first executes only P1 for *r*₁ rounds (with stopping its execution of P2). Note that if a faulty process *p* has a correct process *q* as its neighbor, *p* or *q* can find the inconsistency between them in P1 or P2. During the first *r*₁ rounds (or the recovery time of P1 for *f*₁-faulty configurations (*f*₁ ≥ *f*')), these processes execute only P1, and P1 reaches a legitimate configuration. After that, these processes start their execution of P2 on the correct input from P1. These processes execute only P2 for the *r*₂ rounds (or the recovery time of P2 for *f*₂-faulty configurations (*f*₂ ≥ *f*')). Figure 3 illustrates the outline of the RWFC-LNS strategy.



The features of the local neighborhood synchronizer are summarized as follows. Once initiated, the local neighborhood synchronizer makes the processes within the distance $\max\{c_1, c_2\} + \min\{f_1, f_2\} + 1$ set their timer values to $r_1 + r_2$ and then decrease the values one by one. The decrement of the timer values is executed in a synchronized fashion; the processes keep difference of timer values between neighboring processes at most

one. Even when started from any configuration, the self-stabilizing synchronizer reaches a legitimate configuration (where timer values are synchronously decreased) in $O(r_1 + r_2)$ rounds.

From the above, given an *f*₁-fault-containing protocol P1 and an *f*₂-fault-containing protocol P2, RWFC-LNS provides a min{*f*₁, *f*₂}-fault-containing protocol. The contamination radius of the obtained protocol is $O(\max\{c_1, c_2\} + \min\{f_1, f_2\})$. The recovery time of the obtained protocol is $O(r_1 + r_2)$.

Conclusions

We proposed a novel timer-based fault-containing composition technique RWFC-LNS for fault-containing self-stabilizing protocols that guarantees containment of the effect of faults during the recovery. The proposed composition technique facilitates the design of new fault-containing protocols and enhances reusability of existing fault-containing protocols, which reduces the burden of protocol designers.

The RWFC-LNS technique utilizes the temporal containment property of fault-containing protocols while the previous technique proposed by the authors [3] utilizes the spatial containment. To implement the timers at processes, we designed a local neighborhood synchronizer.

One of the most important applications of the proposed method is ring embedding in an arbitrary network. Ring is one of the most investigated networks in distributed computing and many fault-containing protocols have been designed for rings. The authors [4] proposed a ring embedding on an arbitrary rooted tree that preserves fault-containment property of protocols executed on the embedded ring. We can execute fault-containing protocols designed for rings on an arbitrary network by composing the ring embedding and fault-containing spanning tree construction by the proposed composition technique.

References

- [1] S. Dolev, Self-stabilization, MIT Press, Cambridge, MA, 2000.
- [2] S. Ghosh, A. Gupta, T. Herman, S.V. Pemmaraju, Fault-containing self-stabilizing algorithms, in Proceedings of the 15th Annual ACM Symposium on Principles of Distributed Computing, 1996, pp. 45–54.
- [3] Y. Yamauchi, S. Kamei, F. Ooshita, Y. Katayama, H. Kakugawa, T. Masuzawa, Composition of fault-containing protocols based on recovery waiting fault-containing composition framework, in Proceedings of the 8th International Symposium on Stabilization, Safety, and Security of Distributed Systems, 2006, pp. 516–532.
- [4] Y. Yamauchi, T. Masuzawa, D. Bein, Preserving the fault-containment property of ring protocols executed on trees, The Computer Journal, 52 (4), 2009, pp. 483–498.

Direct Visualization of Secondary Structures of F-actin by Electron Cryomicroscopy

Paper in journals: this is the first page of a paper published in *Nature*.

[*Nature*] 467, 724–728(2010)

LETTER

doi:10.1038/nature09372

Direct visualization of secondary structures of F-actin by electron cryomicroscopy

Takashi Fujii¹, Atsuko H. Iwane¹, Toshio Tanagida¹ & Keiichi Namba¹

F-actin is a helical assembly of actin, which is a component of muscle fibres essential for contraction and has a crucial role in numerous cellular processes, such as the formation of lamellipodia and filopodia^{1,2}, as the most abundant component and regulator of cytoskeletons by dynamic assembly and disassembly (from G-actin to F-actin and vice versa). Actin is a ubiquitous protein and is involved in important biological functions, but the definitive high-resolution structure of F-actin remains unknown. Although a recent atomic model well reproduced X-ray fibre diffraction intensity data from a highly oriented liquid-crystalline sol specimen³, its refinement without experimental phase information has certain limitations. Direct visualization of the structure by electron cryomicroscopy, however, has been difficult because it is relatively thin and flexible. Here we report the F-actin structure at 6.6 Å resolution, made obtainable by recent advances in electron cryomicroscopy. The density map clearly resolves all the secondary structures of G-actin, such as α -helices, β -structures and loops, and makes unambiguous modelling and refinement possible. Complex domain motions that open the nucleotide-binding pocket on F-actin formation, specific D-loop and terminal conformations, and relatively tight axial but markedly loose interprotofilament interactions hydrophilic in nature are revealed in the F-actin model, and all seem to be important for dynamic functions of actin.

Many of the atomic models of F-actin proposed over the years^{3–5} were obtained by maximizing the agreement between experimental intensities of X-ray fibre diffraction and those calculated from a model. However, because the diffraction patterns are cylindrically averaged and layer lines are broadened in an arc owing to the finite disorientation, it is extremely difficult to obtain individual Fourier–Bessel components of the structure factors for three-dimensional (3D) density reconstruction. That is why these analyses have been done by building many models, calculating layer-line intensities and maximizing the agreement between observed and calculated intensities to find a best possible model, except in one case with tobacco mosaic virus⁶. Therefore, there is always some concern as to whether or not such models are unique.

Technical advances in the electron cryomicroscopy (cryoEM) and image analysis of frozen hydrated specimens in recent years have allowed the structural analysis of helical assemblies of biological macromolecules, such as the bacterial flagellar filament, at near-atomic resolution by aligning and averaging tens of thousands of molecular images using helical symmetry^{7–9}. CryoEM image analyses of F-actin have also been carried out but only up to 13 Å resolution^{10,11}, so the atomic model is of limited accuracy in studying the mechanisms of actin polymerization and depolymerization. Because F-actin is a flexible, ribbon-like filament with a diameter of 100 Å and a mass-per-length of 1.5 kDa Å⁻¹, the image contrast of frozen hydrated specimens is markedly lower than that of thicker tubular structures of the flagellar filament (230 Å, 11.0 kDa Å⁻¹) and tobacco mosaic virus (180 Å, 12.6 kDa Å⁻¹), making accurate image alignment and high-resolution analysis extremely difficult. However, recent technical advances¹² have allowed us to obtain a 3D density map of skeletal muscle F-actin at 6.6 Å resolution.

¹Graduate School of Frontier Biosciences, Osaka University, 1-1 Yamadaoka, Suita, Osaka 565-0871, Japan.

724 | NATURE | VOL 467 | 7 OCTOBER 2010

Key to this is our use of an in-column Ω -type energy filter and charge-couple-device (CCD) camera as well as a field-emission gun and a liquid-helium-cooled specimen stage. A remarkable ~5-fold gain in contrast has been achieved by energy filtering, controlling ice thickness and using a specimen temperature of 50 K instead of 4 K (ref. 11). We can now see the two-stranded helical features of F-actin even at small defocus levels (Fig. 1a). The CCD camera made the collections of high-quality images far more efficient, but to avoid undesirable removal of high-resolution contrast by its poor modulation transfer function¹² we used a magnification of 172,000 × (0.87 Å per pixel). We collected 490 such high-quality images in two days. We used a single-particle image analysis method using helical symmetry^{13,14}. Because we fully automated the whole procedure including corrections for the contrast transfer function, the image analysis was completed within two days. The helical symmetry and the axial repeat distance were refined in the iterative process of image analysis and converged to a subunit rotation of -166.6° , corresponding to a helical symmetry of between 28/13 and 13/6 (subunits/turn), and an axial repeat of 27.6 Å. The resolution was 6.6 Å at a Fourier shell correlation of 0.143 (ref. 14; Supplementary Figs 1 and 2). Layer lines are visible out to 6.8 Å in the power spectrum of the 3D reconstruction (Fig. 1b; see also Supplementary Fig. 3). The variance map shows the reliability of the density map as well as the rigid helical backbone of the filament (Supplementary Fig. 4).

Because the resolution was better than that needed to identify individual secondary structures of actin, including loops and an extended amino-terminal chain previously unresolved in the crystal structure (Fig. 2 and Supplementary Movie 1), we were able to build a highly reliable atomic model of F-actin. The situation is analogous to protein crystallography at 3 Å resolution, where side chains can be identified and used to build a reliable atomic model. Although the flexibility of F-actin, especially in its helical order, has been debated over the years¹⁵, the high-resolution map obtained by using over 97% of the collected images indicates that F-actin is not so flexible. Multireference alignment with reference 3D volumes of F-actin with different helical symmetries produced a narrow angular distribution (Fig. 1c), indicating that the twisting variability by thermal motion is less than $\sim 1^\circ$. This also demonstrates the importance of careful cryospecimen preparation with an automated vitrification device (Methods).

To build a reliable atomic model of F-actin, we used FlexEM¹⁶, which refines the atomic model by fitting it into the electron microscopy map by simulated annealing molecular dynamics with stereochemical and non-bonded interaction terms restrained. We used the crystal structure of uncomplexed actin¹⁷ (Protein Data Bank ID, 1J6Z) as the model representing G-actin and divided it into four domains (Fig. 3), which have been conventionally named subdomains¹⁷. We call them domains because domains 1, 3 and 4 have well-defined hydrophobic cores and behave as rigid, independent units on conformational change from G-actin¹⁸ to F-actin (Fig. 3a), as indicated by the small root-mean-squared displacements of C α atoms (Supplementary Table 1). This in turn ensures the correctness and reliability of the present F-actin model. The model and the refinement process are shown in Fig. 2 and Supplementary Movie 2, respectively.

▲2010 Nature Publishing Group. Reprinted with permission from Takashi Fujii et al., Direct visualization of secondary structures of F-actin by electron cryomicroscopy, *Nature*, 467, 724–728(2010).

The following is a comment on the published paper shown on the preceding page.

Direct Visualization of Secondary Structures of F-actin by Electron Cryomicroscopy

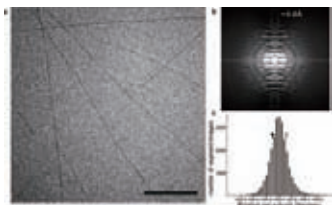
FUJII Takashi and NAMBA Keiichi

(Graduate School of Frontier Biosciences)

Introduction

F-actin is a helical assembly of actin, an essential component of muscle fibers for contraction, and plays crucial roles in numerous cellular processes, such as lamellipodia and filopodia^{1,2}, as the most abundant component and regulator of cytoskeletons by dynamic assembly and disassembly processes. While actin is a ubiquitous protein and is involved in important biological functions, the definitive high-resolution structure of F-actin remains unknown. Although the recent atomic model nicely reproduced X-ray fiber diffraction intensity data from a highly oriented liquid-crystalline sol specimen³, its refinement without experimental phase information has certain limitations. Direct visualization of the structure by electron cryomicroscopy, however, has been difficult due to its relatively thin, flexible structure. CryoEM image analyses of F-actin have also been carried out by many groups in the world over decades but the highest resolution achieved has remained only at 13 Å^{3,4,5}, having limited the accuracy of atomic model to study the mechanisms of actin polymerization and depolymerization. Here we report the F-actin structure at 6.6 Å resolution, made obtainable by recent advances in electron cryomicroscopy. The density map clearly resolves all the secondary structures, such as α -helices, β -structures and loops, having made unambiguous modeling and refinement possible. Complex domain motions that open up the nucleotide binding pocket upon F-actin formation, specific D-loop and terminal conformations and relatively tight axial but markedly loose interprotofilament interactions of hydrophilic nature revealed in the F-actin model all appear to be important for dynamic functions of actin.

Fig.1 High-contrast cryoEM image of F-actin, its power spectrum and angular distribution of rotation per subunit. a, A CCD frame of frozen-hydrated F-actin filaments embedded in vitreous ice film recorded by zero-loss energy-filtered microscopy. The defocus value is 1,500 nm. Scale bar, 100 nm. b, The power spectrum of the 3D reconstruction without imposing helical symmetry. The layer-line is visible out to 6.8 Å. c, Histogram showing the distribution of the rotation angle per subunit at every 0.2° along the 1-start helix of F-actin by multi-reference alignment. The peak is at 166.6°. The 13/6 helix of F-actin corresponds to 166.15° (black arrowhead), and the 28/13 helix to 167.14° (white arrowhead). The 87% fraction of the whole image segments was classified within $\pm 1^\circ$. The angular distribution clearly shows that the twisting variability of F-actin by thermal motion is within $\sim 1^\circ$.



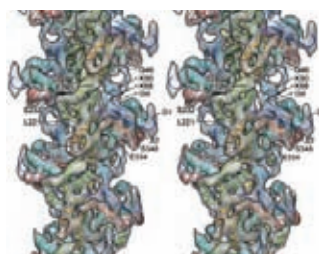
The structural analysis of F-actin by CryoEM

The keys to the success are the use of in-column Ω -type energy filter and CCD camera as well as field emission gun and liquid helium-cooled specimen stage. A remarkable gain in contrast of ~ 5 times has been achieved by energy filtering, controlling ice thickness and a specimen temperature of 50 K instead of 4 K⁶. We can

now see the two-stranded helical features of F-actin even at small defocus levels (Fig. 1a). The CCD camera made high-quality image collection far more efficient, but to avoid undesirable dumping of high-resolution contrast by its poor modulation transfer function⁷, we used a magnification of 172,000 \times (0.87 Å/pixel), which is nearly three-fold higher than that is normally used for imaging on film. We collected 490 such high-quality images in two days. We used a single particle image analysis method using helical symmetry^{6,8}. Since we fully automated the whole procedure including corrections for the contrast transfer function (CTF), the image analysis was completed within two days. The helical symmetry and the axial repeat distance were refined in the iterative process of image analysis and converged to a subunit rotation of -166.6° . Layer lines are visible out to 6.8 Å in the power spectrum of the 3D reconstruction (Fig. 1b). This is a remarkable achievement considering the fact that it used to take months or even longer than a year to carry out 3D image reconstruction at much lower resolution before our own technical improvements that we put into this study.

Since the resolution was better than what is critical to identify individual secondary structures of actin including loops and an extended N-terminal chain that have never been seen in the crystal structures of actin (Fig. 2), we were able to build the atomic model of F-actin far more reliably than before. The situation is analogous to protein crystallography at 3 Å where side chains are identified to build a reliable atomic model. Although the flexibility of F-actin, especially in its helical order, has been debated over the years⁵, the high-resolution map obtained by using over 97% of the collected images indicates that F-actin is not so flexible. Multi-reference alignment with reference 3D volumes of F-actin with different helical symmetries produced a narrow angular distribution (Fig. 1c), indicating that the twisting variability by thermal motion is within $\sim 1^\circ$. This also demonstrates the importance of careful cryo-specimen preparation with an automated vitrification device.

Fig.2 Three-dimensional density map of F-actin with a fitted atomic model in stereo. The atomic model is presented as a $\text{C}\alpha$ ribbon diagram colored in rainbow from the N-terminus in blue to the C-terminus in red. Approximately fifteen subunits of actin are shown to display all the possible azimuthal orientations of actin. Scale bar, 100 Å.



Conformational change from G-actin to F-actin

While the overall conformation of F-actin is similar to the previous ones (Holmes-2003 model⁴ and Oda model³), our present

model shows distinct features in local conformation, such as loops and terminal chains. Even the positions of main chain atoms are distinctly different as indicated by rms deviations of corresponding $\text{C}\alpha$ atoms. Since the nature of conformational change from G-actin to F-actin is of immense importance for biological implications for actin functions, we carefully compared the F-actin structure with G-actin⁹. G-actin can be divided into four domains as labeled D1, D2, D3, D4 in Fig. 3a. While the two major-domains (domains 1-2 and 3-4) are twisted in G-actin, they become flat in F-actin. However, the relative domain motions are more complex than those described previously³. When domain 1 is superposed, domain 2 is tilted towards domain 4 by 10° and towards the outside of F-actin (towards the reader in Fig. 3b) by 20° around the red spear (Fig. 3b and 3c red arrow). Together with the conformational change in D-loop, the slightly bent domain 1-2 in G-actin become significantly flatter in F-actin (Fig. 3c). When domain 3 is superposed, domain 4 is tilted towards the inside of F-actin (away from the reader in Fig. 3e) by 7° (light-blue arrows) around the light-blue spear (Fig. 3e and 3f), making a slightly bent domain 3-4 in G-actin flatter in F-actin. At the same time domain 1 is rotated relative to domain 3 by 13° (Fig. 3g green arrows) around the green spear passing diagonally through domain 4 to the outside of domain 1 (Fig. 3e and 3g).

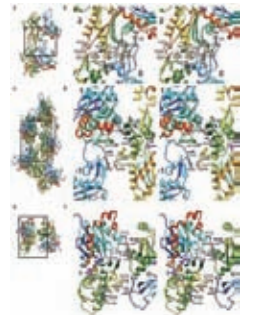
Fig.3 Comparison of actin models in F-actin and the uncomplexed crystal structure. The $\text{C}\alpha$ ribbon diagram in magenta is the atomic model in F-actin, and that in blue is the crystal structure. a, Actin structure was divided into four subdomain D1, D2, D3, D4. b, Superposition of the two structures for each domain. The $\text{C}\alpha$ atoms of residues 34–37 and 54–68 were used for superposition of domain 2. c and d, Domain 1 (labeled D1) is superposed to compare domain 2 (D2) in two different views. Only domains 1 and 2 are colored in c, and shown in d. The solid red spears in c and d are the axis of rotation of domain 2. d is viewed right against the direction of the red spear in c. e, f and g, Domain 3 is superposed to compare domains 4 (D4) and 1 (D1) in two different views. The solid spears in e, f and g are the axes of rotation: light blue for domain 4; green for domain 1. f and g are viewed right against the directions of the light-blue and green spears, respectively. Short arrows in red in c, blue in f and green in g indicate the motions of domain 2 relative to 1, domain 4 relative to 3, and domain 1 relative to 3, respectively.

The detail of subunit-subunit interactions in F-actin

Axial interactions along the protofilament are tight (Fig. 2 and 4a-b). The axial interactions are extensive but not to the extent of the previous model³. The difference is partly due to the distinct D-loop conformation. The axial interactions are mostly electrostatic and hydrophilic albeit there are some hydrophobic interactions. In contrast, interprotofilament interactions are surprisingly modest with only two points of contact (Fig. 2 and 4c-f). One is between the plug in domain 3 and the beginning of D-loop of subunit -1. The main chain oxygen of Ile 267 at the top of this plug may also form a bond with His 173 in domain 3 of subunit 1. This plug has been called “hydrophobic plug” because it was modified to an extended hairpin for hydrophobic interactions with the opposite strand¹⁰. However, the plug conformation observed in the crystal structures is preserved in F-actin (Fig. 2; two actin subunits on the top right), and since the plug forms a salt bridge and hydrophilic interactions with subunits -1 and 1 to stabilize the two-stranded F-actin structure (Fig. 4d), it should be called “hydrophilic plug”. The nature of interactions between actin subunits is mostly electrostatic or

hydrophilic. This explains F-actin depolymerization at concentrated salt solutions¹¹. However, F-actin is not fragile because a number of electrostatic and hydrophilic bonds can make a protein stable in a similar manner to hydrophobic ones.

Fig.4 Axial and lateral interactions of actin subunits in F-actin. a and b, Axial interactions in side view. c and d, Interprotofilament interactions in side view. e and f, Interprotofilament interactions in end-on view from the bottom (barbed-end side). a, c and e are guides to show the portions displayed in b, d and f in stereo, respectively. Only subunits 0 and 1 are shown in e and f. The models are shown as $\text{C}\alpha$ ribbon diagram colored in rainbow as in Fig. 2 with relevant side chains in stick representation and colored according to the element: carbon, grey; nitrogen, blue; and oxygen, red. The side chain conformation of K113, H173 and E195 was manually modified to indicate their potential involvement in the interprotofilament interactions.



CryoEM image analysis has advanced enough to allow the visualization of side chains for icosahedral viruses¹² and chaperonins, but high-contrast images due to their large sizes are essential for accurate image alignment for high-resolution analysis. It is therefore thought that high-resolution analysis of small or thin objects, such as F-actin, is extremely difficult due to their intrinsically low image contrast. We have demonstrated that our improved cryoEM technologies now allow us to visualize the secondary structures of such thin objects as F-actin within a few days from image data collection to 3D image reconstruction. It would be fairly easy to reveal the structures of F-actin in complex with actin binding proteins, such as myosin, troponin and tropomyosin, in similar details, and such structures will bring us deep insights into the mechanisms of muscle contraction and regulation as well as those of cellular motility and morphogenesis. There is also room for further improvement to reach atomic resolution. The present work has opened up the whole new opportunity to look into cellular mechanisms essential for the activities of life.

References

- [1] Pollard, T. D. & Borisy, G. G. Cellular motility driven by assembly and disassembly of actin filaments. *Cell* **112**, 453-465 (2003).
- [2] Carlrier, M. F. & Pantaloni, D. Control of actin assembly dynamics in cell motility. *J. Biol. Chem.* **282**, 23005-23009 (2007).
- [3] Oda, T., Iwasa, M., Aihara, T., Maeda, Y., & Narita, A. The nature of the globular- to fibrous-actin transition. *Nature* **457**, 441-445 (2009).
- [4] Holmes, K. C. *et al.* Electron cryo-microscopy shows how strong binding of myosin to actin releases nucleotide. *Nature* **425**, 423-427 (2003).
- [5] Galkin, V. E., Orlova, A., Cherepanova, O., Lebart, M. C. & Egelman, E. H. High-resolution cryo-EM structure of the F-actin-fimbrin/plastin ABD2 complex. *Proc. Natl Acad. Sci. USA* **105**, 1494-1498 (2008).
- [6] Fujii, T., Kato, T., & Namba, K. Specific Arrangement of α -helical coiled coils in the core domain of the bacterial flagellar hook for the universal joint function. *Structure* **17**, 1-9 (2009).
- [7] Sander, B., Golas, M. M. & Stark, H. Advantages of CCD detectors for de novo three-dimensional structure determination in single-particle electron microscopy. *J. Struct. Biol.* **151**, 92-105 (2005).
- [8] Egelman, E.H. A robust algorithm for the reconstruction of helical filaments using single-particle methods. *Ultramicroscopy* **85**, 453-463 (2000).
- [9] Otterbein, L. R., Graceffa, P. & Dominguez, R. The crystal structure of uncomplexed actin in the ADP state. *Science* **293**, 708-711 (2001).
- [10] Holmes, K. C., Popp, D., Gebhard, W. & Kabsch, W. Atomic model of the actin filament. *Nature* **347**, 44-49 (1990).
- [11] Nagy, B. & Jencks, W. P. Depolymerization of F-actin by concentrated solutions of salts and denaturing agents. *J. Am. Chem. Soc.* **87**, 2480-2488 (1965).
- [12] Zhang X, Jin L, Fang Q, Hui WH, Zhou ZH. 3.3 Å cryo-EM structure of a nonenveloped virus reveals a priming mechanism for cell entry. *Cell* **141**, 472-482 (2010).